

Ammonium Sulfate: Equilibrium and Metastability Phase Diagrams from 40 to -50 °C

Jun Xu,[†] Dan Imre,* Robert McGraw, and Ignatius Tang

Brookhaven National Laboratory, Upton, New York 11973-5000

Received: April 21, 1998; In Final Form: July 20, 1998

The temperature-dependent phase diagrams, from 40 to -50 °C, of the binary $(\text{NH}_4)_2\text{SO}_4/\text{H}_2\text{O}$ system are derived from data collected in a low-temperature, single-levitated-particle apparatus. The conditions of vapor pressure, temperature, and composition, at which particle phase transitions occur along the path of increasing relative humidity, define the equilibrium phase diagram, whereas the set of conditions that induce transitions in the reverse direction defines the metastability phase diagram. A new, stable crystalline phase of $(\text{NH}_4)_2\text{SO}_4 \cdot 4\text{H}_2\text{O}$ is identified. Below -19.35 ± 0.05 °C, the anhydrous $(\text{NH}_4)_2\text{SO}_4$ –ice eutectic point, ammonium sulfate does not deliquesce as the RH is increased but instead undergoes a solid–solid phase transition to form a tetrahydrate phase. $(\text{NH}_4)_2\text{SO}_4 \cdot 4\text{H}_2\text{O}$ incongruently melts at -19.35 °C. Equilibrium phase transition, as well as metastable to stable phase transitions, for this system are mapped out, and the derived phase diagrams allow for prediction of the composition and phase of $(\text{NH}_4)_2\text{SO}_4$ aerosols under the full range of atmospheric conditions and paths. Present observations are in excellent agreement with previous data.

1. Introduction

Atmospheric aerosols play important roles in visibility degradation and climate change.¹ Aerosols impact the global climate directly, by the scattering of significant portions of solar radiation to space, and indirectly, as they control cloud optical properties and formation.² The indirect effect of aerosols on cloud coverage and cloud optical properties^{3,4} still remains the largest uncertainty in the estimate of anthropogenic emissions and their impact on climate. Aerosols and cloud droplets also provide sites for important heterogeneous reaction pathways, which alter atmospheric chemistry and composition.⁵ For these reasons, processes related to atmospheric aerosols have recently taken center stage in atmospheric science research.

Sulfates are the most important class of anthropogenic atmospheric aerosols. They are the product of the oxidation of SO_2 to H_2SO_4 .^{5,6} In the remote atmosphere, where aerosol concentrations are low, sulfuric acid molecules nucleate to form new particles.⁷ In polluted environments, where particles are abundant, sulfuric acid molecules tend to condense on preexisting particles. In the polluted lower troposphere, where ammonia concentrations tend to be high, sulfuric acid particles can be neutralized all the way to ammonium sulfate, while at higher altitudes and in the presence of lower ammonia concentrations, aerosols may be only partially ammoniated.⁸ Recent experimental results, however, which study contrail and cirrus cloud formation, show that ammoniated sulfate aerosols can be transported to the upper troposphere by convection.⁹

In this paper we present the ammonium sulfate water phase diagram which we derived from observations of single levitated particles over a broad range of temperatures and vapor pressures. Droplet growth and evaporation studies of single levitated aerosol particles, including $(\text{NH}_4)_2\text{SO}_4$, have been carried out in our laboratory since 1976 by Tang et al.^{10–14} A reproduction of one of these room-temperature experiments on $(\text{NH}_4)_2\text{SO}_4$ particles is illustrated in Figure 1. The change in particle mass, as a result of water vapor condensation (open symbols) or evaporation (filled symbols), is expressed as moles of water

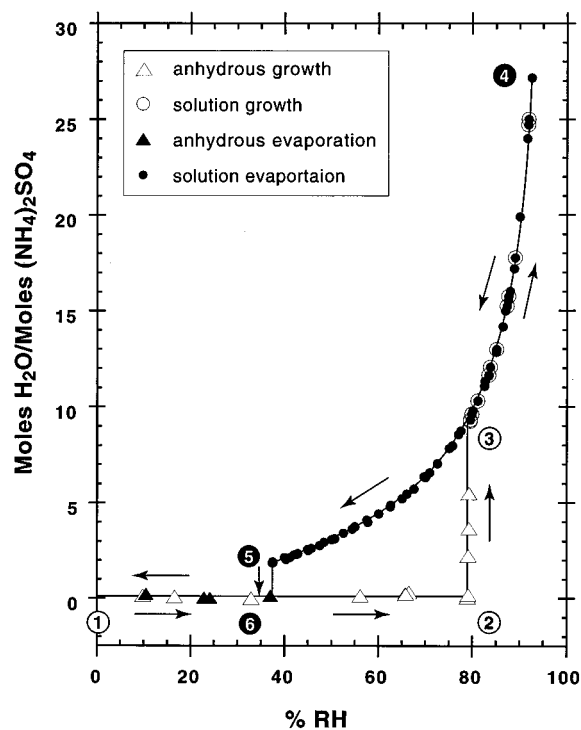


Figure 1. Ammonium sulfate growth and evaporation cycle at 25 °C (reproduced from Tang and Munkelwitz¹²). Open symbols designate the growth phase; filled symbols designate evaporation. The growth cycle starts at point 1 with an anhydrous ammonium sulfate crystal that remains in that phase up to the deliquescence point 2. Path 2 to 3 represents the deliquescence process, during which the particle absorbs the exact amount of water required to form a saturated solution phase (in this case 9.56) to point 3. The droplet continues to grow as RH further increases beyond the deliquescence point (3 to 4). During the reverse cycle (4 to 3) the solution droplet passes the deliquescence point 3; there, instead of undergoing a transition back to the solid phase, the particle remains a homogeneous solution phase to point 5. At point 5 it effloresces suddenly and loses of all its water to return to anhydrous crystal form. The region 3–5 represents the supersaturated solution.

per moles of solute and plotted as a function of relative humidity (RH). As RH increases, the solid $(\text{NH}_4)_2\text{SO}_4$ particle remains

[†] Also at Institute for Terrestrial and Planetary Atmospheres, State University of New York.

unchanged (1 to 2), until RH reaches 80%. At this point the particle deliquesces spontaneously (2 to 3) to form a saturated solution droplet that contains 9.6 water molecules per molecule of solute. Point 2 defines the deliquescence point of ammonium sulfate at room temperature. The droplet continues to grow as RH further increases beyond the deliquescence point (3 to 4). During evaporation, the solution droplet passes the deliquescence point without a phase change and becomes a highly supersaturated metastable droplet (4 to 5). Finally, crystallization occurs at 37% RH (5 to 6). Similar results were also reported by Richardson et al. (1984),¹⁵ Rood et al. (1989),¹⁶ Cohen et al. (1987),¹⁷ and Chan et al. (1992).¹⁸

A low-temperature, single-particle levitation system, recently developed in our laboratory, allowed us to extend earlier studies¹⁰ and explore the behavior of this binary system over an expanded temperature range. In this paper, we report the first, complete single-particle-derived $(\text{NH}_4)_2\text{SO}_4/\text{H}_2\text{O}$ equilibrium and metastability phase diagrams, as well as the discovery of a new, low-temperature crystalline $(\text{NH}_4)_2\text{SO}_4 \cdot 4\text{H}_2\text{O}$ phase. A brief description of the experimental system is provided in section 2. Section 3 discusses the experimental results. Section 4 is devoted to the phase diagrams and also provides some thermodynamic parameters for the saturated solution.

2. Experimental Section

A detailed description of this low-temperature single-particle apparatus will be given in a separate publication, here we provide a brief outline of its principal components.

a. The Chamber. Figure 2 is a schematic representation of the low-temperature apparatus. The single-particle levitation cell is constructed of copper, to ensure thermal equilibration, and is suspended inside an insulating vacuum shroud. The cell maintains thermal contact with a liquid nitrogen bath through heat-transfer straps (ST). Two resistive heating elements (H) allow for precise temperature control in the range of -140 to 30 °C. The system can be operated in fixed or scanning temperature modes. Cell temperature is monitored on the outside, in contact with the cell wall, and inside, above and below the particle (T_m). All reported data points correspond to conditions in which the temperatures, above and below the particle, are within 0.25 °C. The system is calibrated against ice pressure at an estimated absolute accuracy of ± 0.2 °C.

b. The Particle Trap. A DC potential is impressed symmetrically on the top (t) and bottom (b) sheets of the two hyperboloidal electrodes. The symmetry of the DC potential is maintained by a series of variable potentiometers over a range up to 20 V. An AC potential is impressed upon the hyperboloidal conductor (ac). The AC potential a varies over a range of 500 V. Under optimal conditions, an electrically charged aerosol particle can be contained for over a week at the null point in space by an alternating electric field, where the particle is balanced against gravity by a DC potential, V_{DC} . The theory and design of the single-particle levitation cell, also known as an electrodynamic balance, have been treated fully by others.^{11–14,19–21}

A charged particle is obtained from a doubly filtered, 4 wt % solution of known composition. That solution is loaded into a particle gun, from which a single particle is produced by impact and injected into the trap. The particle is captured in dry nitrogen at the center of the cell by the tweaking of AC and DC voltages applied to the electrodes. The diameter of the dry particle is typically between 5 and 10 μm . A linear, vertically polarized HeNe laser beam penetrates the cell through a side window and is focused on the particle at all times. The intensity of the scattered light is continuously monitored at 90°

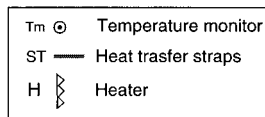
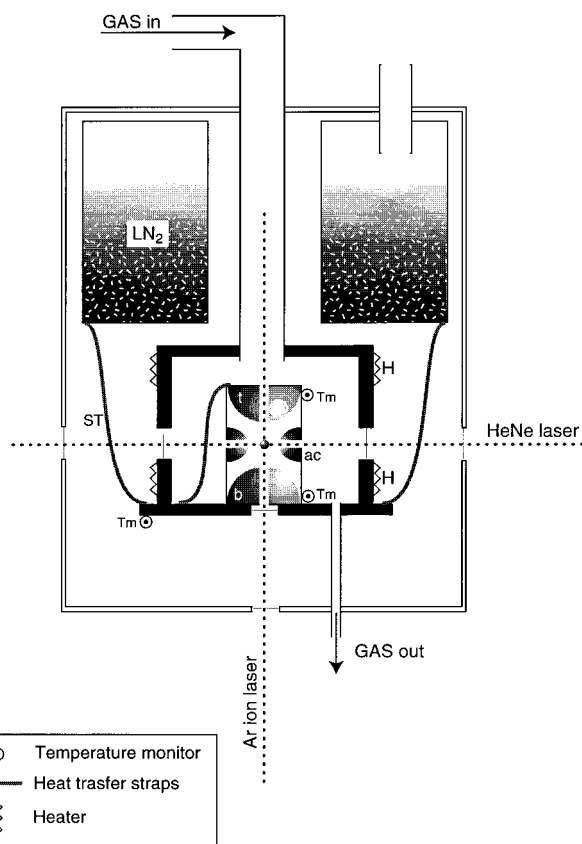


Figure 2. Schematic representation of the low-temperature cell. The particle, shown at the intersection of the two laser beams, is levitated at the center of the electrostatic trap created by the fields generated by the AC electrode (ac) and balanced against gravity by the DC field created between the top (t) and bottom (b) electrodes. The interaction chamber, shown in solid, made of copper, is thermally connected by heat-transfer straps (ST) to the liquid nitrogen reservoir (LN_2). Heaters (H) are used to control the temperature, which is monitored at three points, above, below, and outside (T_m).

to the laser path. Phase transitions (solid–liquid) are readily detected from changes in Mie scattering. Since this single-particle levitation system is capable of operating over a wide temperature range and under controlled gas phase conditions, it provides a very powerful tool for the study of physical and chemical properties of particles under realistic atmospheric conditions.

$(\text{NH}_4)_2\text{SO}_4/\text{H}_2\text{O}$ particles were generated and captured at -10 °C. The system was then closed and pumped to a pressure lower than 10^{-7} Torr. For constant temperature experiments, the chamber temperature was set, the chamber was filled with ~ 10 Torr of dry nitrogen, and the DC voltage (V_0) required to position the dry particle at the null point was noted. V_0 is the voltage corresponding to the mass of pure $(\text{NH}_4)_2\text{SO}_4$ particle. After V_0 was measured, the buffer gas was removed, water vapor was slowly introduced into the system, and the particle's mass and its phase were monitored as a function of water vapor pressure. No buffer gas was used at pressures lower than ice, and the total pressure was assumed to be that of water.

In the present study we also conducted a set of experiments designed to establish the properties of the system at temperatures and water pressures where the solution is in equilibrium with ice. Here $(\text{NH}_4)_2\text{SO}_4$ particles were deliquesced at a constant temperature below 0 °C, and the water vapor pressure was increased, until ice plated on the cell walls. To facilitate equilibrium 5 Torr of nitrogen was added as buffer gas. At this point the cell was sealed and the particle composition was

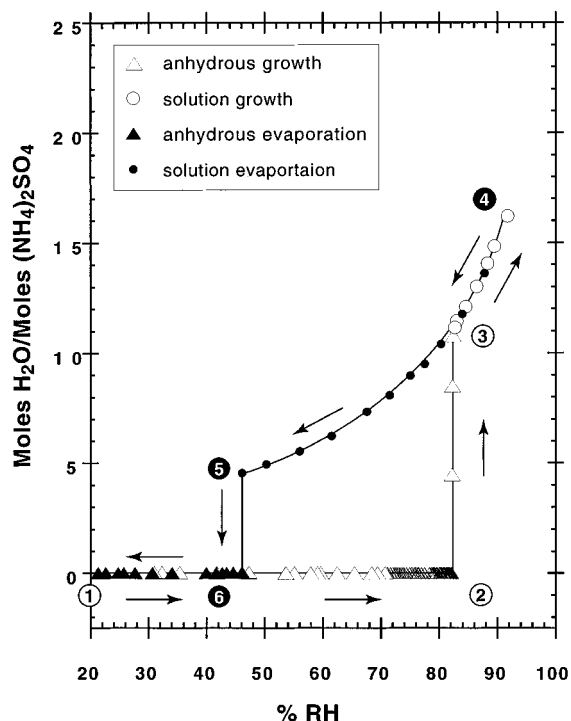


Figure 3. Ammonium sulfate growth and evaporation cycle at -9.4 °C. Symbols are identical to those used for the 25 °C cycle shown in Figure 1. The deliquescence point 2 at this temperature is slightly higher than that observed at 25 °C, and the saturated solution is composed of 11 waters for each ammonium sulfate molecule. The highest RH data point (4) corresponds to ice pressure. Note that while the deliquescence RH at this temperature is only $\sim 2\%$ higher than that at 25 °C, the efflorescence point is 9% higher.

monitored as the temperature was reduced. This procedure ensured that the system was maintained at equilibrium with ice throughout the entire path.

3. Results

The data reported here is a product of a large number of experiments on many particles. In Figures 3 and 4 we provide an example of two such experiments, one at constant temperature and the second a hybrid experiment, consisting of a constant temperature hydration followed by a temperature scan along the ice line.

Figure 3 illustrates a hydration/dehydration cycle as a plot of mole ratio $\text{H}_2\text{O}/(\text{NH}_4)_2\text{SO}_4$ vs relative humidity at a constant temperature of -9.4 °C. The cycle shown in this figure is qualitatively very similar to the room-temperature cycle shown in Figure 1. In the path 1 to 2 in Figure 3, the particle exists as anhydrous $(\text{NH}_4)_2\text{SO}_4$, which is the stable phase up to $\text{RH} = 82.2\%$ (point 2), the deliquescence RH at -9.4 °C. At this point, the particle rapidly absorbs water and forms a saturated $(\text{NH}_4)_2\text{SO}_4$ solution droplet (path 2 to 3), with about 11 water molecules per $(\text{NH}_4)_2\text{SO}_4$ solute molecule. As RH is increased beyond the deliquescence point, the particle takes up water, which causes the $(\text{NH}_4)_2\text{SO}_4$ concentration drop (point 4). On the reverse path, where RH is decreased, the particle remains in the liquid phase far beyond the deliquescence point and produces a supersaturated solution. The dehydration path (4 to 5) exhibits typical hysteresis, and from point 3 to 5 the particle is in a metastable supersaturated state. At this temperature (-9.4 °C), the efflorescence point (5) is at $\text{RH} = 46\%$ and the particle suddenly crystallizes to form anhydrous $(\text{NH}_4)_2\text{SO}_4$, by shedding of all excess water. Note that while the deliquescence point of the present run, at -9.4 °C, is only 2.2% different in RH from

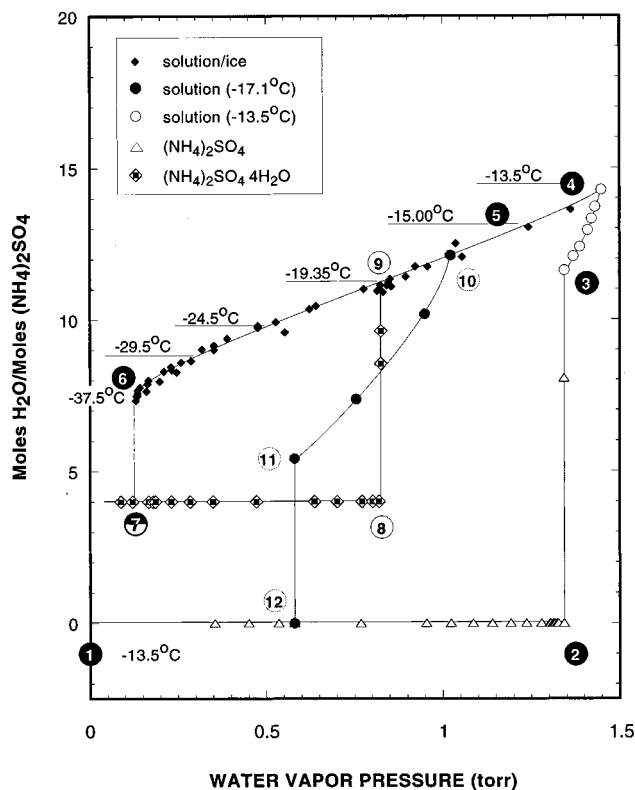


Figure 4. Composite cycle, designed to obtain information along the ice/solution equilibrium line. The constant temperature growth path (1–4) carried out at -13.5 °C is analogous to that shown in Figures 1 and 3. To bring the water pressure in the chamber into equilibrium with ice, the chamber temperature was lowered to -15.0 °C while the water inlet valve was kept fully open. Constant pressure is indicative of equilibrium with ice, and the path 5 to 6 represents the cooling cycle along the ice line. At a temperature of -37.5 °C (point 6), the solution droplet suddenly transforms to a solid particle composed of ~ 7.5 waters for each ammonium sulfate molecule. At constant temperature and pressure, the composition of this solid changes gradually by a loss of water (path 6 to 7), until it reaches its final tetrahydrate state. The tetrahydrate phase is stable to any further temperature changes up to -19.35 °C. Here the particle melts and absorbs water to form a homogeneous solution at point 9. To close the cycle the temperature is elevated to -17.5 °C (point 10) and kept constant, while the chamber pressure is decreased. The evaporation cycle (10 to 11) produces the original anhydrous crystal by efflorescence (point 12).

that at 25 °C, the efflorescence RH has increased from 37% to 46%. This large temperature effect on efflorescence RH is a consistent feature in this system.

Figure 4 illustrates a hybrid cycle that was designed to study the properties of this system along the water–ice frost line. This cycle starts with the hydration of an anhydrous particle (path 1 to 2), at a constant temperature of -13.5 °C. At this temperature the deliquescence point (2 to 3) is at 1.35 Torr ($\text{RH} = 82.4\%$) and the saturated solution droplet composition is 11.6 water molecules per $(\text{NH}_4)_2\text{SO}_4$ solute molecule. The path 3 to 4 produces a dilute solution where the water pressure is that of ice at -13.5 °C. To ensure that the system is at the ice frost point, the temperature is decreased to -15.0 °C while the water vapor source remains open. A waiting period of a few hours allows the system to reach equilibrium, as noted by constant temperature and water pressure equal to that of ice. At the end of the waiting period the chamber walls are coated with ice, and as long as the temperature is not allowed to rise above -15.0 °C the water vapor pressure in the cell is equal to and thereafter controlled by the vapor pressure of ice. To facilitate thermal equilibrium the cell is filled with 5 Torr of nitrogen. The

temperature-dependent composition of the $(\text{NH}_4)_2\text{SO}_4$ solution that is at equilibrium with ice is determined by the expression of particle mass as a function of temperature (path 5 to 6). As shown in Figure 4, the $(\text{NH}_4)_2\text{SO}_4$ particle in this run remained as a homogeneous supercooled solution droplet down to -37.5 °C (point 6). At that temperature it suddenly transformed into a solid particle composed of approximately 7.5 water molecules per molecule of ammonium sulfate. When maintained for over 0.5 h at constant temperature and pressure, the particle lost additional water and attained its final stable composition of $(\text{NH}_4)_2\text{SO}_4 \cdot 4\text{H}_2\text{O}$ (path 6 to 7). While the path 4 to 6 is perfectly reproducible, the efflorescence temperatures of the particles were found to vary between -41 and -36.5 °C.

The tetrahydrate phase, once formed, remains stable as the temperature is varied along the ice line up to -19.35 °C (path 7 to 8). At -19.35 °C the particle incongruently melts into the anhydrous phase and its saturated solution. Since -19.35 °C is the eutectic point between ice and the anhydrous phase, it is also the anhydrous deliquescence temperature at ice pressure, which is the water vapor pressure throughout this experiment. Consequently, the melt composed of the anhydrous particle and its $(\text{NH}_4)_2\text{SO}_4$ saturated solution promptly deliquesces to form a single-phase droplet (8 to 9). $(\text{NH}_4)_2\text{SO}_4 \cdot 4\text{H}_2\text{O}$ was also observed to melt at -19.35 °C under lower-than-ice pressure. Under these conditions the melting particle promptly transforms into the anhydrous phase.

The two distinct pathways that the system takes following incongruent melting at ice and lower-than-ice pressures delineate some of the sharp differences between bulk and particle behavior. In particle form the system must make a choice between an all liquid state—for pressures equal to or higher than ice, and a purely solid state—for pressures lower than ice. In contrast, when a bulk sample of $(\text{NH}_4)_2\text{SO}_4 \cdot 4\text{H}_2\text{O}$ incongruently melts at -19.35 °C, it produces a mixed phase of an anhydrous precipitate in a saturated solution.

As part of our routine quality assurance, we require that all reported data derive from experiments in which closure was demonstrated. To ensure that the data is free from artifacts such as charge loss or contamination, we end every experiment at its starting point. To close the cycle presented in Figure 4, melting and deliquescence were followed by a slight increase in temperature to -17.5 °C (path 9 to 10) and a dehydration at constant temperature (path 10 to 11 to 12). At point 11 the particle effloresces to complete the cycle at the anhydrous phase (point 12).

The tetrahydrate phase can also be produced by a direct anhydrous to tetrahydrate transition. These experiments are carried out under nonequilibrium conditions, in which the temperature is maintained at less than -19.35 °C and the water pressure momentarily increased above the equilibrium ice vapor pressure. At the point where the water pressure is increased to the expected deliquescence point of the anhydrous phase, we observe a phase change. It can be described qualitatively as a partial deliquescence, the end result of which is the absorption of four water molecules by the anhydrous phase and the formation of $(\text{NH}_4)_2\text{SO}_4 \cdot 4\text{H}_2\text{O}$.

Once produced, and as long as the temperature is kept below -19.35 °C, the tetrahydrate phase does not revert to the anhydrous phase, even when the pressure is reduced to 10^{-7} Torr and maintained there for several days. This behavior appears to be a unique property of aerosols. As a general rule, phase transitions induced by an increase in RH take place at equilibrium, while those induced by a decrease in RH take place far from equilibrium, from a metastable to a stable phase. In

particular, the persistence of crystalline hydrates at water vapor pressures far below the equilibrium pressure appears to be commonplace. Similar observations were made in the case of $\text{NH}_4\text{HSO}_4 \cdot 8\text{H}_2\text{O}$ and $\text{LiClO}_4 \cdot \text{H}_2\text{O}$.^{22,23} The persistence of water-rich phases deep into the metastable region may have important implications for a variety of atmospheric processes.

The combination of data as presented in Figures 1, 3, and 4 of the vapor pressure temperatures and compositions where deliquescence occur with an increase in RH provides an equilibrium phase diagram. Similarly, the conditions of phase transformations that are induced with a decrease in RH provide the data for the construction of a metastability phase diagram. Both types of phase diagrams are presented below.

4. Discussion

a. Phase Diagram. 1. Equilibrium Phase Diagram. Figure 5a shows the $(\text{NH}_4)_2\text{SO}_4/\text{H}_2\text{O}$ equilibrium phase diagram in the composition/temperature domain. The pure solution region is indicated by horizontal lines. The observed deliquescence points (open circles) define the $(\text{NH}_4)_2\text{SO}_4$ –solution coexistence line. The ice–solution coexistence line down to -37.5 °C is labeled with filled diamonds. The data points extending beyond the eutectic point (EU) at -19.35 represent the supercooled solution at equilibrium with ice. The tetrahydrate incongruent melting point at -19.35 °C is represented by the horizontal line (IM). The data points labeled with filled squares represent the temperatures in which the tetrahydrate is formed.

Figure 5b shows the same phase diagram as in Figure 5a, presented in the water vapor pressure/temperature domain as a plot of $\log(P_w)$ vs $1000/T$. The symbols in this figure are consistent with those in Figure 5a. Also shown in Figure 5b are the water–ice frost line and the liquid water vapor pressure as functions of $1/T$. The anhydrous deliquescence points form a nearly straight line in this plot.

The observed anhydrous to tetrahydrate solid–solid phase transitions are labeled as checked squares. These transitions were induced at temperatures below -19.35 °C through a rapid increase of water pressure to above that of ice. The data, although not as precise as the rest of the measurements in this study, suggest that this transition occurs along the anhydrous deliquescence line. The light scattering pattern during this transition indicates a partial solid-to-liquid transition that is immediately followed by the formation of a new solid, whose composition is consistent with that of the tetrahydrate. The incongruent melting point (IM) is shown as a vertical line in this representation, and the tetrahydrate stability region lies to the right of that line. It is interesting to note that the hydrated solid forms for ammonium sulfate as well as for ammonium bisulfate, tetrahydrate, and octahydrate, respectively, form upon cooling a solution droplet along the ice line, as well as through solid–solid phase transitions.

2. Metastability Phase Diagram. Because phase metastability in aerosols is the “rule”, rather than the exception, the phase diagram above is a map in pressure, temperature, and composition of the conditions at which phase transitions take place with an increase in RH alone. In contrast, phase transformations along the reverse path, almost always commence from highly metastable states. This is a manifestation of a free energy barrier that must be overcome in order to form a critical nucleus.¹¹

The value of a similar map for phase transitions along the path of decreasing RH would depend on the degree to which these metastable-to-stable phase transitions are reproducible. In a recent, similar study on the phase transformations of am-

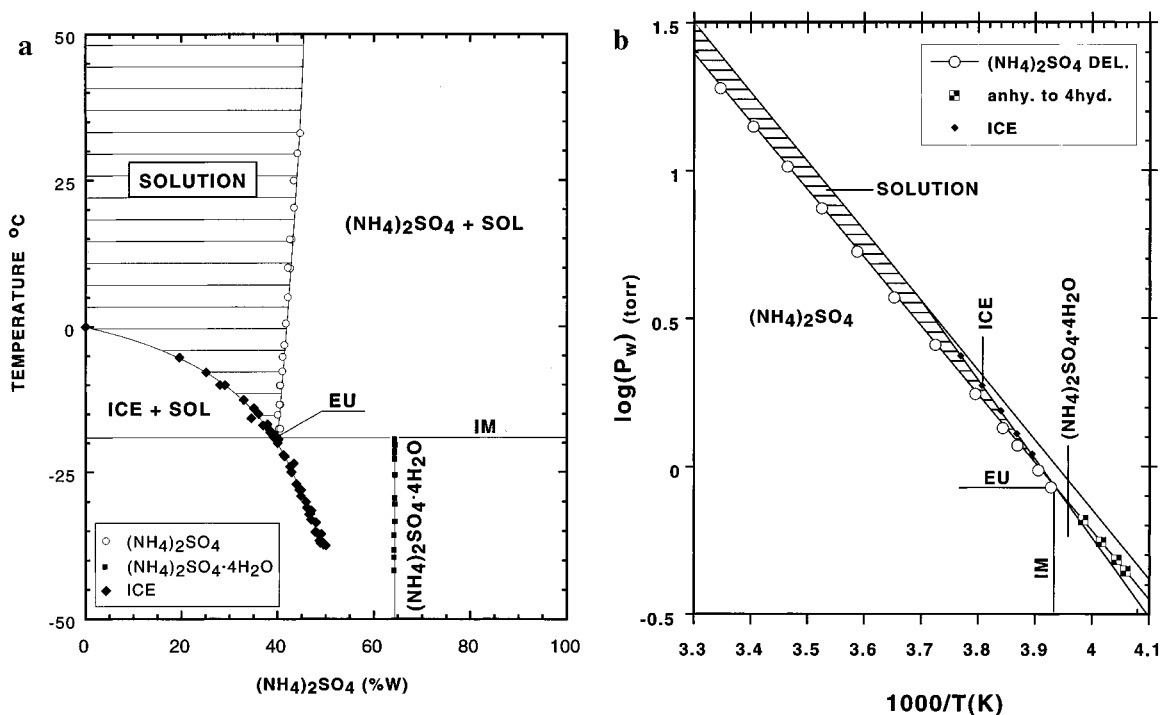


Figure 5. (a) Ammonium sulfate/water equilibrium phase diagram, expressed in temperature vs composition. The pure solution is represented by the striped region. The ice–solution equilibrium data points are shown as filled diamonds and the anhydrous solution equilibrium points as open circles. The eutectic point at -19.35 °C is labeled by EU. The composition of the tetrahydrate phase and its incongruent melting point are shown as well. All the data points below the eutectic temperature correspond to a metastable solution whose vapor pressure equals that of ice. (b) Ammonium sulfate/water equilibrium phase diagram as $\log(P_w)$ vs $1/T$ domain. The pure solution is represented by the striped region. The ice–solution coexistence line is shown as filled diamonds and the anhydrous–solution equilibrium, i.e., the deliquescence points, as open circles. The eutectic point at -19.35 °C (3.94 in the figure) and ice pressure is labeled by EU. The region where the tetrahydrate is the stable phase is indicated as well. The checkered squares represent the anhydrous to tetrahydrate transition points.

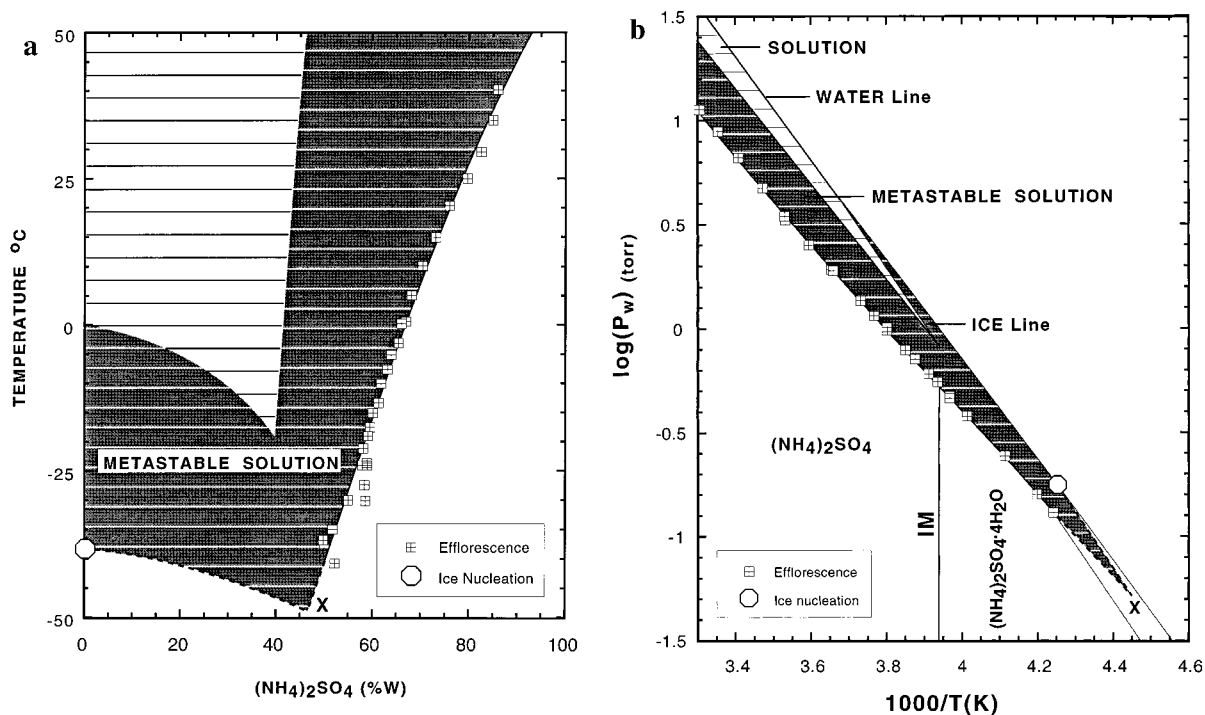


Figure 6. (a) Ammonium sulfate/water metastability phase diagram in temperature vs composition domain. The pure solution equilibrium region is represented by the open striped region, while the metastable solution is shown as the gray striped area. All observed efflorescence points are indicated with tiled squares. Homogeneous ice nucleation from pure water is labeled with the octagon. The dashed line is based on an extrapolation described in the text. X marks the lowest temperature where solution microdroplets can be found. (b) Ammonium sulfate/water metastability phase diagram in the $\log(P_w)$ vs $1/T$ domain. The pure equilibrium solution region is represented by the open striped region, while the metastable solution is shown as the gray striped area. All observed efflorescence points are indicated with tiled squares. Homogeneous ice nucleation from pure water is labeled with the octagon. The dashed line is based on an extrapolation described in the text. X marks the lowest temperature where solution microdroplets can be found.

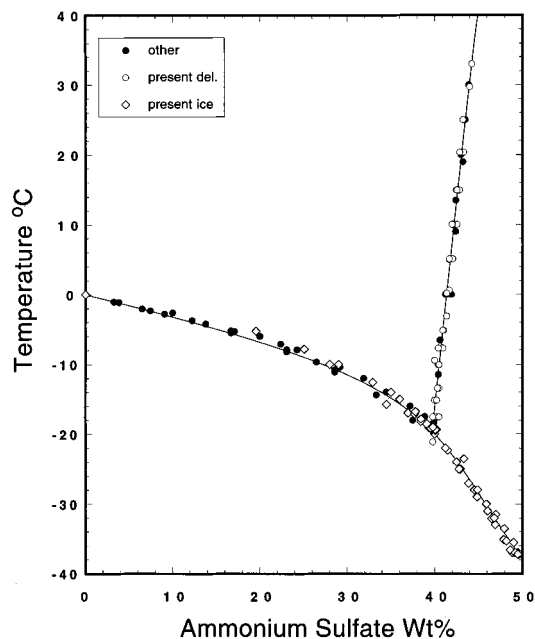


Figure 7. Comparison between our current data, previously published data, and latest model, all showing good agreement as far as the saturated solution composition is concerned.

monium bisulfate, we have shown that in that system, metastable-to-stable phase transitions take place within a very narrow range of reproducible and therefore predictable conditions.²² The present experimental results on ammonium sulfate exhibit similar behavior. The efflorescence transitions take place along reasonably well-defined lines, repeatedly producing the same phase within a very narrow range of pressures and temperatures. We interpret these observations to be indicative of a sharp onset of nucleation, as supersaturation or undercooling is increased beyond the threshold for the first observable nucleation to occur. The lines in these phase diagrams connect points of approximately equal nucleation rates, which for our experimental system is $\sim 1 \times 10^8$ to 1×10^9 events/cc s.

We construct the $(\text{NH}_4)_2\text{SO}_4/\text{H}_2\text{O}$ metastability phase diagram by combining the conditions (temperature, water vapor pressure, and droplet composition) where the efflorescence transitions have been observed. The metastability phase diagram in temperature/composition as well as pressure/temperature domains is shown in Figure 6a,b, respectively. The metastable solution region is represented by the gray area, and the metastable solution-to-anhydrous transitions are marked by tiled squares. These comprise all of the efflorescence points that can be accessed by our current experimental system. The data suggest a slightly increasing spread in efflorescence conditions with a decrease in temperature. The three lowest temperature data points are all on the ice line.

The remainder of the metastable-to-stable transitions take place under conditions that require the gas phase to be supersaturated with respect to ice formation, and these conditions are inaccessible to our current apparatus. The well-known homogeneous nucleation of water to ice at -38 °C is labeled by the octagon in both figures. This section of the metastability phase diagram is constructed by a linear extrapolation—in $\log(p_w)$ vs $1/T$ space—of the observed efflorescence transition at temperatures below 0 °C to extend the ammonium sulfate nucleation line beyond the frost line. To derive the ice nucleation line, we assume that it is linear in the same representation and that the slope is the same as that of pure ice.

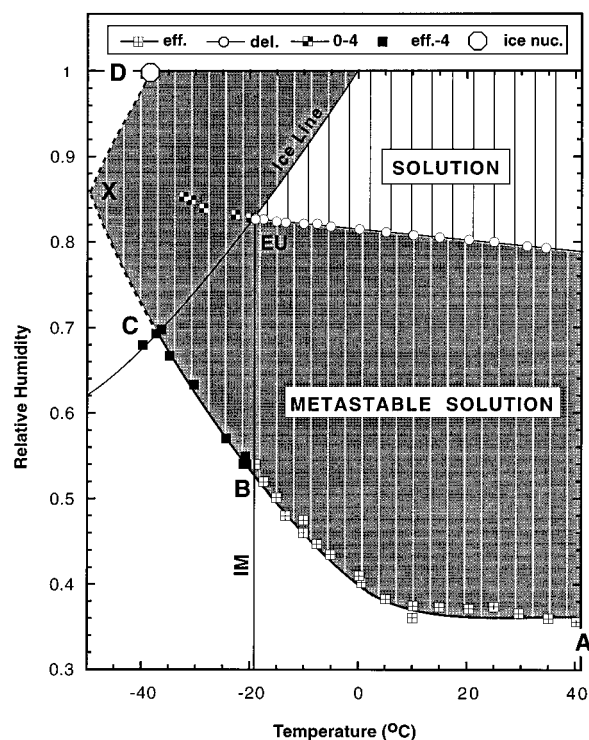


Figure 8. Summary of all observed phase transitions in the binary ammonium sulfate/water system in a RH vs temperature plot. The pure equilibrium solution region is represented by the open striped region, while the metastable solution is shown as the gray striped area. The deliquescence points form an almost straight line in this domain and indicate only a slight change in RH with temperature. The efflorescence points, labeled with tiled squares, represent anhydrous formation. The filled squares correspond to efflorescence transitions that form the tetrahydrate phase. The dashed line is based on an extrapolation described in the text. X marks the lowest temperature where solution microdroplets can be found. The checked squares indicate anhydrous-to-tetrahydrate solid–solid phase transitions. The points labeled A, B, C, X, and D mark boundaries along the nucleation path A to D where phase changes take place. They are described in the text and listed in Table 1.

The dashed lines in Figure 6a,b indicate the two extrapolated lines, and the intersection between them at -49 °C is labeled by an X. This is the lowest temperature at which micron-size liquid ammonium sulfate droplets can be found.

The region defined by the line indicating the incongruent melting point at -19.35 °C ($1000/T = 3.94$ K⁻¹) marks the stability region of the tetrahydrate. We find that once the tetrahydrate phase is formed and as long as the temperature remains below -19.35 °C this phase remains stable for several days even if water pressures are reduced to 10^{-7} Torr. This finding is consistent with our previous observations on $\text{LiClO}_4 \cdot \text{H}_2\text{O}$ ¹³ and $\text{NH}_4\text{HSO}_4 \cdot 8\text{H}_2\text{O}$.²²

The path taken to reach the gray region at temperatures between -19.35 and -49 °C determines its phase; metastable solution, ice, anhydrous, or tetrahydrate phases can all be found.

Figure 7 shows the good agreement between our current observations and data obtained from past “bulk” experiments.²⁴ This agreement underlines the utility of single-particle experiments for the construction of such phase diagrams. The advantage that single-particle experiments offer is their ability to investigate homogeneous phase transitions in an environment free of walls and impurities. Such systems also allow one to construct, without additional effort, pressure/temperature phase diagrams.

TABLE 1: Metastable-to-Stable Transitions in the $(\text{NH}_4)_2\text{SO}_4$ Water System

region ^a	temp, °C	RH, %	final phase ^b	nucleus	gas phase ^c
A–B	40 to –19.35	35–53	AS	$(\text{NH}_4)_2\text{SO}_4$	–
B–C	–19.35 to –38	53–68	AST	$(\text{NH}_4)_2\text{SO}_4$	–
C–X	–38 to –49	68–85	AST, ice	$(\text{NH}_4)_2\text{SO}_4$	+
X–D	–49 to –38	85–100	ice, AST	ice	+

^a The regions are defined according to Figure 8. ^b AS, $(\text{NH}_4)_2\text{SO}_4$; AST, $(\text{NH}_4)_2\text{SO}_4 \cdot 4\text{H}_2\text{O}$. ^c A + in this column indicates that the vapor phase is metastable with respect to ice formation.

A summary of all observed phase transitions (deliquescence, efflorescence, and solid–solid) are shown in Figure 8, as a plot of RH vs temperature. The symbols remain consistent with those in Figure 6a,b. This is the most natural representation of the data for atmospheric systems. It shows the deliquescence transitions as open circles and illustrates the very slight changes in deliquescence with temperature. In sharp contrast, efflorescence transitions are shown to be highly temperature-dependent. In this figure the metastable-to-stable transitions occur along the line A–B–C–X–D. Table 1 lists the temperatures, RHs, and the solids that form in each of these sections. With the aid of Figure 8 and Table 1 below, one can predict the phase of an ammonium sulfate particle under any atmospheric condition. It is important to keep in mind that the region C–X–D is based on an approximate extrapolation and that line A–D is expected to be size-dependent.

b. Thermodynamic Properties of the Saturated Solution.

1. $(\text{NH}_4)_2\text{SO}_4$ –Solution Coexistence Line. Measurement of the vapor pressure over a saturated solution provides information on the enthalpies of that solution. To derive these quantities we follow Tang and Munkelwitz,²⁷ where the change in \ln RH with respect to temperature is expressed as:

$$\frac{d \ln RH}{dT} = \frac{x_2}{x_1} \left(\frac{\Delta H_s}{RT^2} \right) \quad (1)$$

x_1/x_2 is the molar ratio (solvent/solute), and ΔH_s is the integral heat of solution.

The molar ratio at the deliquescence point can be expressed as a polynomial in T :

$$x_2/x_1 = a + bT + cT^2 \quad (2)$$

Equation 3 below is obtained when eq 2 is substituted into eq 1 and the resulting expression then integrated from a reference temperature T^* :

$$\ln \left[\frac{\text{RH}(T)}{\text{RH}(T^*)} \right] = \frac{\Delta H_s}{R} \left[a \left(\frac{1}{T} - \frac{1}{T^*} \right) - b \ln \frac{T}{T^*} - c(T - T^*) \right] \quad (3)$$

where T^* is defined as a fixed reference temperature, in our case $T^* = 298.2$ K.

The coefficients in eq 2 are derived from a quadratic fit to the observed molar ratio. A plot of the observed x_2/x_1 in the present set of experiments (open circles) and that previously available (filled circles) is shown as a function of temperature in Figure 9 where the solid curve represents the quadratic fit to the combined data, for a total of 35 points, whose parameters are given in Table 2.

2. Ice–Solution Coexistence Line. The data presented in Figure 5a above can also be used to derive an empirical relationship between temperature and composition along the

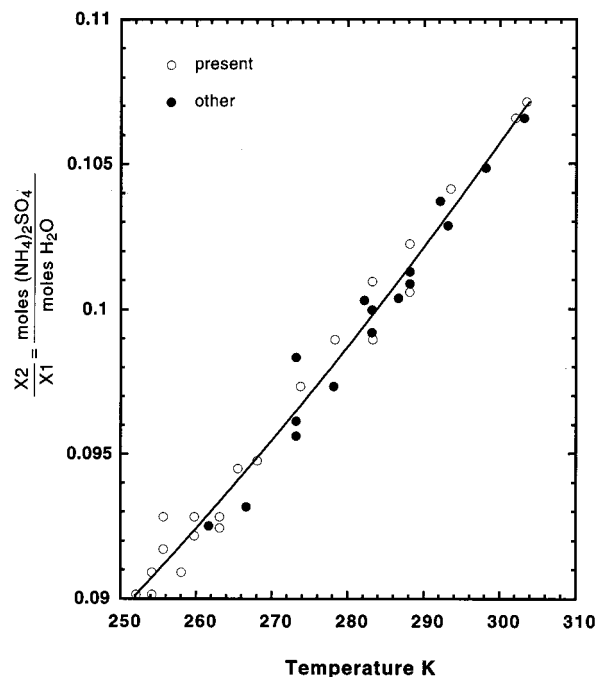


Figure 9. Plot of the composition of the saturated solution, in moles of solute per mole of water, as a function of temperature. The line is a quadratic fit to the data; its coefficients are given in Table 2 and are used to derive the heat of solution (see text for details). The fit is to the combined present and past data for a total of 35 data points.

TABLE 2: Empirical Parameters for Eq 3

$\Delta H_s/R$	a	b	c
606.1	0.0778	-1.83×10^{-4}	9.21×10^{-7}

ice–solution coexistence line. To derive this line we combine our current experimental data with previously available results, for a total of 85 data points over a temperature range from 0 to -37.5 °C. Equation 4 describes the empirical relationship between temperature, in degrees Kelvin, and solution composition (W), in weight percent:

$$T(K) = 273.15 - 0.282W - 5.1529 \times 10^{-3}W^2 + 3.537 \times 10^{-4}W^3 - 9.02 \times 10^{-6}W^4 \quad (4)$$

c. **Estimating Uncertainties.** Figure 9 can be used to estimate the uncertainties in the composition measurements. On the scale of this figure the ± 0.2 K uncertainty in temperature is insignificant and the scatter in the data is, therefore, entirely due to the composition measurements. The uncertainty is derived by calculating the rms deviation about the line given in eq 2. When translated to ammonium sulfate weight percent, it yields $\pm 0.5\%$.

To estimate the uncertainty in RH measurements, we use the deliquescence data shown in Figure 8. The spread of observed deliquescence RH about the line in eq 3 implies a random error on the order of $\pm 0.2\%$ in RH. By comparison with previous measurements, we estimate an absolute accuracy of $\pm 0.5\%$ in RH. At lower temperatures and lower water pressures the error is closer to $\pm 1\%$.

5. Conclusion

These data provide strong support for the utility of single-particle experiments for the generation of complete and accurate

thermodynamic phase diagrams. The first study for which we have used this approach was of ammonium bisulfate—a system for which virtually no previous data has been available for comparison. In contrast, for the case of (NH₄)₂SO₄/H₂O, the equilibrium phase diagram has been previously well-characterized, and we found almost perfect agreement between published bulk data and our derived equilibrium phase diagram.

The equilibrium and metastability phase diagrams in the region of 40 to −50 °C of the binary (NH₄)₂SO₄/H₂O system have been reported in this paper for the first time, and a new, low-temperature crystalline phase composed of (NH₄)₂SO₄·4H₂O was discovered. We were able to extend the data and estimate the conditions necessary for ice nucleation as well. Since no data is currently available for this region of the phase diagram, our approximation of it can serve as a guide. This extrapolation suggests that −50 °C closely approximates the low-temperature limit in which liquid microparticles can exist. On the basis of these phase diagrams, it is possible to predict the phase and composition, for a given path, of any (NH₄)₂SO₄ aerosol under any thermodynamic condition. The RH vs temperature representation of the complete phase diagram appears to be most suitable for atmospheric applications.

The reproducibility/predictability of metastable-to-stable phase transition in ultrapure systems is an important issue with implications in a variety of fields. The systems that we have examined (ammonium sulfate, ammonium bisulfate, and sulfuric acid) all indicate highly reproducible, metastable-to-stable phase transformations and therefore lend credence to the utility of the corresponding phase diagrams. It is important to recognize that metastability phase diagrams are somewhat dependent on particle size: i.e., small particles show deeper supersaturations for similar observation times than do larger ones. In a separate publication we show that it is possible, on the basis of the present study, to effectively express relationships between particle size and nucleation conditions.

Acknowledgment. We thank Professor Anthony Wexler for useful discussion. This work was supported by the U.S. Department of Energy (Contract DE-AS02-76H00016).

References and Notes

- (1) Baker, M. B. *Science* **1997**, *276*, 1072–1078.
- (2) Charlson, R. J.; Schwartz, S. E.; Hales, J. M.; Cess, R. D.; Coakley, J. A.; Hansen, J. E.; Hofmann, D. J. *Science* **1992**, *255*, 423–430.
- (3) Schwartz, S. E.; Andreae, M. O. *Science* **1996**, *272*, 1121–1122.
- (4) Ravishankara, A. R. *Science* **1997**, *276*, 1058–1064.
- (5) Twomey, S. *Atmospheric Aerosol*; Elsevier Scientific Publishing: Dordrecht, New York, 1977.
- (6) Jensen, E. J.; Toon, O. B. et al. *J. Geophys. Res.* **1994**, *99*, 10421.
- (7) Collett, J. L.; Bator, A., Jr.; Xin, R.; Demoz, B. B. *Geophys. Res. Lett.* **1994**, *21*, 2393–2396.
- (8) Sheridan, P. J.; Brock, C. A.; Wilson, J. C. *Geophys. Res. Lett.* **1994**, *21*, 2587–2590.
- (9) Tabazadeh, A. *J. Geophys. Res.* **1997**, submitted.
- (10) Tang, I. N. *J. Aerosol Sci.* **1976**, *7*, 361.
- (11) Tang, I. N.; Munkelwitz, H. R. *J. Colloid Interface Sci.* **1984**, *98*, 430.
- (12) Tang, I. N.; Munkelwitz, H. R. *J. Geophys. Res.* **1994**, *99*, 18801–18808.
- (13) Tang, I. N.; Fung, K. H.; Imre, D. G.; Munkelwitz, H. R. *Aerosol Sci. Technol.* **1995**, *23*, 443–453.
- (14) Tang, I. N. *J. Geophys. Res.* **1997**, *102*, 1883–93.
- (15) Richardson, C. B.; Spann, J. F. *J. Aerosol Sci.* **1984**, *15*, 563–571.
- (16) Rood, M. J.; Shaw, M. A.; Larson, T. V.; Covert, D. S. *Nature* **1989**, *337*, 537–539.
- (17) Cohen, M. D.; Flagan, R. C.; Seinfeld, J. H. *J. Phys. Chem.* **1987**, *91*, 4563–4574.
- (18) Chan, C. K.; Flagan, R. C.; Seinfeld, J. H. *Atmos. Environ.* **1992**, *26A*, 1661–1673.
- (19) Wuerker, R. F.; Shelton, H.; Langmuir, R. V. *J. Appl. Phys.* **1959**, *30*, 342–349.
- (20) Frickel, R. H.; Schaffer, R. E.; Stamatoff, J. B. National Technical Information Service, Technical Report ARCSL-TR-77041; Chem. Syst. Lab., Aberdeen Proving Ground, MD, 1978.
- (21) Yong, P. K.; Pun, B. K. L.; Chan, C. K.; Flagan, R. C.; Seinfeld, H. *Aerosol Sci. Technol.* **1994**, *20*, 275–284.
- (22) Imre, D. G.; Xu, J.; Tang, I. N.; McGraw, R. *J. Phys. Chem.* **1997**, *101*, 4191–4195.
- (23) Imre, D. G.; Xu, J.; Tridico, A. C. *Geophys. Res. Lett.* **1997**, *24*, 69–72.
- (24) Timmermans, J. *Physico-Chemical Constants of Binary Systems in Concentrated Solutions*; Interscience Publishers: New York, 1960; Vol. 4, pp 619–625.
- (25) Clegg, S. L.; Brimblecombe, P. *J. Chem. Eng. Data* **1995**, *40*, 1079–1090.
- (26) Clegg, S. L.; Brimblecombe, P.; Wexler, A. S. *J. Phys. Chem.* **1997**, submitted.
- (27) Tang, I. N.; Munkelwitz, H. R. *Atmos. Environ.* **1993**, *27A*, 467–473.